

Dynamical Pattern Formation without Self-Attraction in Quorum-Sensing Active Matter: The Interplay between Nonreciprocity and Motility

Yu Duan¹, Jaime Agudo-Canalejo¹, Ramin Golestanian^{1,2,*}, and Benoît Mahault^{1,†}

¹Max Planck Institute for Dynamics and Self-Organization (MPI-DS), 37077 Göttingen, Germany

²Rudolf Peierls Centre for Theoretical Physics, University of Oxford, Oxford OX1 3PU, United Kingdom

 (Received 13 June 2023; accepted 31 August 2023; published 3 October 2023)

We study a minimal model involving two species of particles interacting via quorum-sensing rules. Combining simulations of the microscopic model and linear stability analysis of the associated coarse-grained field theory, we identify a mechanism for dynamical pattern formation that does not rely on the standard route of intraspecies effective attractive interactions. Instead, our results reveal a highly dynamical phase of chasing bands induced only by the combined effects of self-propulsion and nonreciprocity in the interspecies couplings. Turning on self-attraction, we find that the system may phase separate into a macroscopic domain of such chaotic chasing bands coexisting with a dilute gas. We show that the chaotic dynamics of bands at the interfaces of this phase-separated phase results in anomalously slow coarsening.

DOI: [10.1103/PhysRevLett.131.148301](https://doi.org/10.1103/PhysRevLett.131.148301)

Active systems are driven out of equilibrium at the level of their microscopic constituents. Since activity may arise in various forms, including particle motility [1], local generation of nonconservative forces [2,3] and torques [4,5], growth [6], or sustained chemical reactions [7], the active matter field is rapidly expanding in multiple directions [8]. Recently, the generation of interactions breaking action-reaction symmetry [9–13] as a paradigm for activity has received increasing attention. Such nonreciprocal interactions occur in a variety of contexts, including particles interacting through a nonequilibrium medium [14–21], or via social forces [22–24].

Because of connections built with non-Hermitian physics [25,26], nonreciprocity has been argued to constitute a generic route for the emergence of steady states breaking time reversal symmetry (TRS) [10–12,18,27–30]. Examples include rotating chiral phases in flocking systems involving multiple species [12], or traveling patterns in phase-separating mixtures [10,11]. The latter are described by the nonreciprocal Cahn-Hilliard (NRCH) model [10,11], which generalizes the Cahn-Hilliard theory of phase separation [31] by including a nonequilibrium chemical potential with antisymmetric couplings between species. Importantly, the NRCH model predicts that preconditions for the emergence of TRS broken phases are the presence of intraspecies attraction that drives demixing, as

well as chasing interspecies interactions [10,11]. In addition to dynamical patterns, the similarity between the NRCH model and reaction-diffusion equations [32,33] has led to additional connections such as the presence of Turing-like instabilities [27,34].

A model mechanism for self-organization in motile active matter are quorum-sensing interactions. Quorum sensing mediated by chemical signals is, for example, known to drive swarming and pattern formation in bacterial populations [35–37]. Collective aggregation was moreover shown to arise in suspensions of light-activated colloids whose motility is locally regulated by their density via feedback control loops [23,38,39]. Often, quorum-sensing interactions are modeled as a direct response of particle motility to local density variations [40–42]. Despite their simplicity, minimal quorum-sensing models are able to capture complex collective behaviors [23,37]. A notable example is the motility induced phase separation (MIPS), whose origin is rooted in the effective attraction induced by the self-inhibition of motility [40]. In addition, nonreciprocal couplings naturally arise when multiple species exhibit quorum sensing with asymmetric responses [17,43], thus without resorting to explicit nonreciprocal pairwise forces [44–46]. For strong nonreciprocity and in the phase separation regime, related models were shown to lead to TRS broken phases in qualitative agreement with the picture provided by the NRCH model [16,17,43].

In this Letter, we study a binary model of quorum-sensing self-propelled particles in two dimensions. Our simulations reveal the presence of thin traveling bands even in the absence of intraspecies couplings. Instead, and as confirmed by the associated coarse-grained field theory, they arise from a new mechanism relying only on self-propulsion and chasing interactions. In large systems, these

Published by the American Physical Society under the terms of the Creative Commons Attribution 4.0 International license. Further distribution of this work must maintain attribution to the author(s) and the published article's title, journal citation, and DOI. Open access publication funded by the Max Planck Society.

bands self-organize into a spatiotemporal chaotic phase that we find to be involved in phase-separated configurations at moderate self-attraction. We show that this phase-separated phase coarsens with a scaling exponent distinct from that of standard MIPS [47–50].

Description of the model.—We consider a dynamics where the position \mathbf{r}_i and orientation $\hat{\mathbf{u}}_i = (\cos \theta_i, \sin \theta_i)$ of particle i from species $S \in \{A, B\}$ evolve at time t according to

$$\dot{\mathbf{r}}_{i,S} = v_S[\tilde{\rho}_A, \tilde{\rho}_B]\hat{\mathbf{u}}_{i,S}, \quad \dot{\theta}_{i,S} = \sqrt{2D_r}\xi_i(t). \quad (1)$$

ξ_i is a Gaussian white noise with zero mean and unit variance, while D_r denotes the corresponding rotational diffusivity assumed equal for the two species. Because of quorum sensing, the self-propulsion velocity v_S in Eq. (1) depends on the coarse-grained density fields $\tilde{\rho}_S(\mathbf{r}, t)$ measured over a finite interaction scale R via a short-ranged kernel $\hat{w}(r)$, whose expression is given in Appendix A. The linear stability analysis performed below reveals that, approximating $\tilde{\rho}_S(\mathbf{r}, t) \simeq \rho_S(\mathbf{r}, t)$ with $\rho_S(\mathbf{r}, t) \equiv \sum_i \delta[\mathbf{r} - \mathbf{r}_{i,S}(t)]$, the emergence of patterns from the dynamics described by (1) is controlled by the dimensionless couplings $\eta_{SS'}(\rho_A, \rho_B) \equiv \rho_S \partial \ln(v_S) / \partial \rho_{S'}$. For $\eta_{SS'} < 0$, a particle from species S moves slower in higher S' density regions, leading to an effective attraction via motility inhibition. In turn, $\eta_{SS'} > 0$ makes S particles spend less time in regions of high S' density, such that motility activation amounts to an effective repulsion. The sign of η_{SS} thus determines whether the effective interaction between particles of same species S is attractive (repulsive), as a result of the self-inhibition (self-activation) of their motilities. For multiple species, nonreciprocity arises whenever $\rho_{S'}\eta_{SS'} \neq \rho_S\eta_{S'S}$, such that the dynamics (1) cannot be coarse-grained to an effective equilibrium field

theory [43]. In particular, effective chasing interactions between species A and B are achieved when $\eta_{AB}\eta_{BA} < 0$.

For simplicity, we consider $v_S(\rho_A, \rho_B) = v_0 L_{SS'}(\rho_A) L_{SB}(\rho_B)$, where $L_{SS'}(x) > 0$ is a logistic function such that v_S varies monotonously with ρ_A and ρ_B . The values of the couplings $\eta_{SS'}$ can then be varied changing either the values of the densities $\rho_{A,B}$, or the shape of the curves $L_{SS'}$. For convenience, we define a reference value ρ_0 such that $v_S(\rho_0, \rho_0) = v_0$ while $\eta_{SS'}^0 \equiv \eta_{SS'}(\rho_0, \rho_0)$ is the value at which $|L'_{SS'}|$ reaches its maximum. Rescaling space and time, we set $R = 1$ and $v_0 = 1$ so that the remaining control parameters of the microscopic model are the mean particle densities $\{\bar{\rho}_S\}$, the nominal couplings $\{\eta_{SS'}^0\}$, and D_r . We moreover define the Péclet number $\text{Pe} \equiv v_B(\bar{\rho}_A, \bar{\rho}_B)/D_r$ as a measure of the self-propulsion strength, while the parameter $\chi \equiv \eta_{AB}(\bar{\rho}_A, \bar{\rho}_B)\eta_{BA}(\bar{\rho}_A, \bar{\rho}_B)$ is used to quantify nonreciprocity. All simulations are performed in periodic domains of size $L_x \times L_y$, with total particle numbers ranging from $N = 10^4$ to 10^7 . Additional details about the microscopic model are given in Appendix A.

Traveling patterns induced by chasing interactions.—To start with, we fix the mean particle densities $\bar{\rho}_S = \rho_0$, such that the couplings $\eta_{SS'}$ evaluated at $\bar{\rho}_{A,B}$ are given by $\eta_{SS'}^0$ and $\text{Pe} = v_0/D_r$. For $\text{Pe} \ll 1$ or $|\chi| \ll 1$, our observations are in line with predictions from the NRCH model [10,11,27]. Namely, if either of η_{AA}^0 or η_{BB}^0 are sufficiently negative, systems initialized in the homogeneous state are unstable. For $\chi > 0$, this instability leads to the phase separation of one of the two species, or demixing. For negative χ and small systems, on the other hand, nonreciprocity gives rise to the formation of system-spanning traveling bands rich in either of the two species and chasing each other [Fig. 1(a) and Supplemental Movie (SMov) 1 [51]]. As this TRS broken phase mainly relies on the presence of two phase-separated domains whose cohesion is maintained by self-inhibition, TRS can be

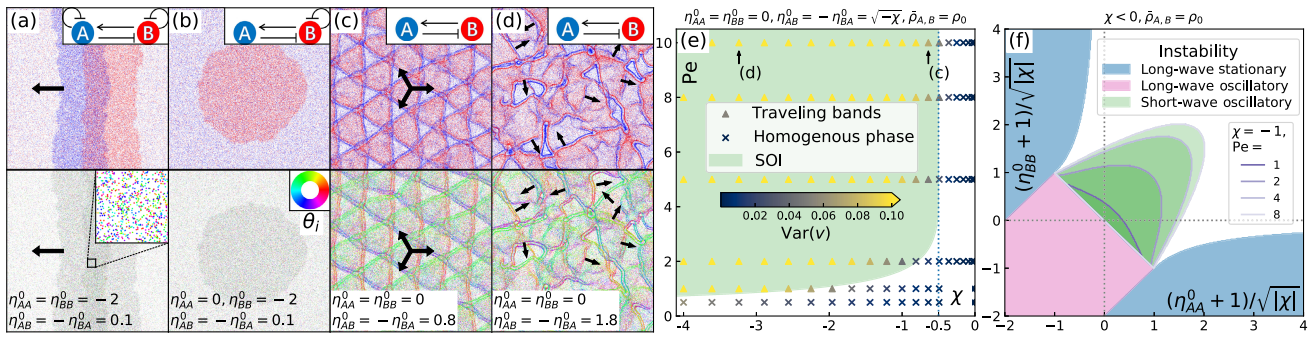


FIG. 1. (a)–(d) Representative simulation snapshots for strong [(a),(b)] and vanishing [(c),(d)] motility self-inhibition in the presence of chasing interactions ($\chi < 0$). The top (bottom) row shows the particles color-coded by their species (polarity orientation), while the thick arrows indicate the traveling direction of the patterns. The enlargement in (a) illustrates how disordered configurations appear in gray. The top captions give a graphical representation of the interaction rules with arrows (bars) denoting motility activation (inhibition). Parameters: $\bar{\rho}_{A,B} = \rho_0 = 80$, $\text{Pe} = 10$, and $L_x = L_y = 40$. (e) $\text{Var}(v)$ (see definition in the text) as function of χ and Pe in the vanishing self-inhibition regime, triangles and crosses indicate points where traveling bands and the homogeneous phase are observed. The green shaded region marks the domain of existence of SOI. (f) Typical linear stability diagram for $\chi < 0$ and $\bar{\rho}_{A,B} = \rho_0$.

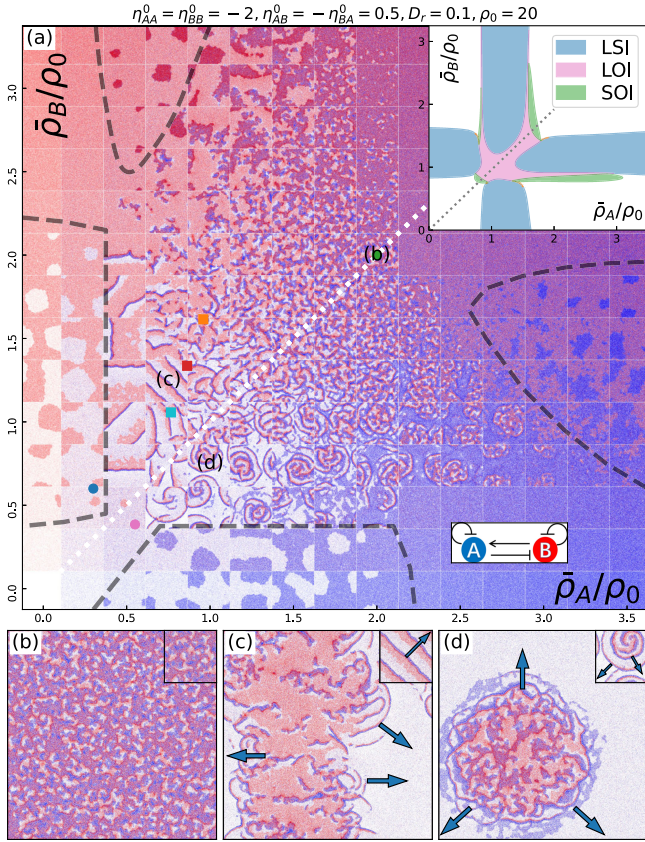


FIG. 2. (a) Snapshots from particle-based simulations in the composition plane in square domains of size $L_x = 40$. The regions of static phase separation are indicated by the dashed lines as guides to the eye. Solid squares and dots respectively mark the compositions used to analyze the profiles of Figs. 3(a)–3(c) and coarsening in Fig. 3(e). Inset: the corresponding linear stability diagram. (b)–(d) Simulations in square domains of size $L_x = 160$, each with the same composition as its top right inset where $L_x = 40$.

restored when one or both species see their self-coupling vanish, as shown in Fig. 1(b).

Strikingly, for $\chi < 0$ and Pe and $|\chi|$ large enough we find traveling patterns arising even at weak or vanishing self-attraction. These patterns take the form of thin chasing bands that for small $|\chi|$ and moderate system size self-organize into a superposition of regular arrangements traveling along different directions [Fig. 1(c) and SMov 1]. Such structure is however rather fragile such that increasing $|\chi|$ [Fig. 1(d)], or in presence of moderate self-inhibition of motilities, it is destabilized and replaced by a chaotic chasing bands (CCB) phase [Fig. 2(b)].

Contrary to the regime of strong motility self-inhibition, the cohesion of the chasing bands here is ensured by the combined effects of Pe and $\chi < 0$. For weak or vanishing self-attraction, traveling bands can only exist if particles inside them move coherently over large distances, as evidenced by the local polarization shown in the bottom row of Figs. 1(c) and 1(d). This feature, which is absent in

strongly self-attracting mixtures [bottom row of Figs. 1(a) and 1(b)], remarkably arises despite the absence of explicit aligning interactions between particle velocities [Eq. (1)]. The residual particle flux to the outside of the bands induced by rotational noise is then balanced by the effect of nonreciprocal interspecies couplings. To understand this, let us consider the case of Figs. 1(c) and 1(d) where species A inhibits the motility of B particles and is activated by them. A cluster of A particles traveling in the gas locally slows down B particles, so that they aggregate at its rear. In the case of vanishing self-attraction, B particles can then follow the A cluster only when they move in the same direction. Similarly, the motility activation of A particles provoked by a B cluster leads them to reside at its front so long as they move in the same direction. This emergent noise rectification mechanism relying on chasing interactions allows the AB cluster pair to continuously recruit particles from the gas. To confirm this picture, we define the system- and time-averaged speed variance $\text{Var}(v) \equiv \langle \langle |\dot{\mathbf{r}}_i|^2 \rangle_i - \langle |\dot{\mathbf{r}}_i \rangle_i^2 \rangle_t$, which is nonzero only in the presence of motility induced patterns. Scanning the $(-\chi, \text{Pe})$ plane at $\eta_{AA}^0 = \eta_{BB}^0 = 0$, Fig. 1(e) shows that the CCB phase—whose onset is characterized by an abrupt growth of $\text{Var}(v)$ —is found when both self-propulsion and non-reciprocity are sufficiently strong.

Mesoscopic description and linear stability analysis.— To get a theoretical understanding of the onset of CCB, we derived the coarse-grained description of the microscopic model. The full derivation uses standard coarse-graining techniques and is detailed in Appendix B. It leads to a pair of equations for the noise-averaged particle density and polarity. Linearizing these equations around their solution with homogeneous densities $(\bar{\rho}_A, \bar{\rho}_B)$ and vanishing polarities, we find that its stability is determined by five parameters: η_{AA} , η_{BB} , χ , Pe , and $\sigma_v \equiv v_A/v_B$, where v_S and $\eta_{SS'}$ are evaluated at $(\bar{\rho}_A, \bar{\rho}_B)$. Taking $\sigma_v = 1$ (see Ref. [51] for a discussion of the general case leading to similar results), the eigenvalue controlling the stability is $\lambda(q) = -(q/2)\gamma + (q/2)\sqrt{\gamma^2 - 2\mu + 2\sqrt{\alpha}}$, where q denotes the wave number of the perturbation while $\gamma(q) \equiv (\text{Pe}q)^{-1} + \text{Pe}q/16$, $\mu \equiv 1 + \frac{1}{2}(\eta_{AA} + \eta_{BB})$, and $\alpha \equiv \chi + \frac{1}{4}(\eta_{AA} - \eta_{BB})^2$.

For $\alpha > 0$, λ is real as $q \rightarrow 0$ and a long-wave stationary instability (LSI) arises when $\mu < \sqrt{\alpha}$, i.e., $\mu < 0$ or $(1 + \eta_{AA})(1 + \eta_{BB}) < \chi$. On the other hand, $\alpha = 0$ corresponds to an exceptional point [10] such that for $\alpha < 0$, the imaginary part of $\lambda(q)$ is always nonzero, while its real part $\Re(\lambda)$ becomes positive if and only if [51]

$$2\mu\gamma^2(q) + \alpha = 2\mu \left(\frac{1}{\text{Pe}q} + \frac{\text{Pe}q}{16} \right)^2 + \alpha < 0. \quad (2)$$

For $\alpha < 0$ and $\mu < 0$ the condition (2) is always true down to $q = 0$, giving rise to a long-wave oscillatory instability (LOI). The emergence of LSI and LOI are thus both mainly

controlled by the intraspecies couplings, such that these instabilities may arise at arbitrary small $|\chi|$ and their range of existence is insensitive to Pe .

Equation (2) moreover shows that for $\alpha < 0$ and $\mu > 0$, although $\Re(\lambda)$ is negative as $q \rightarrow 0$, it may turn positive at finite q when $\gamma^2(q) < -\alpha/2\mu$. As such a scenario can only happen when λ is complex, it is associated to a short-wave oscillatory instability (SOI). This is in contrast with the NRCH model [10,11,27] or reaction-diffusion systems [52] for which SOI is absent in binary mixtures. In the limit $\eta_{AA} = \eta_{BB} = 0$ of vanishing self-couplings, the condition for SOI reduces to $\chi < -\frac{1}{2}$ [dotted line in Fig. 1(e)], while the lowest unstable wave number is given by $\text{Pe}^2 q_c^2 = -32(1 + 4\chi + 8\sqrt{(1/2 + \chi)\chi})$. Using the interaction range $R = 1$ as a natural lower cutoff for the admissible values of q_c^{-1} , we thus get a line in the (χ, Pe) plane that defines the boundary of the instability region shown in Fig. 1(e), and which qualitatively agrees with the numerical simulations of the microscopic model. We furthermore summarize the linear stability results for $\chi < 0$ in the diagram of Fig. 1(f) drawn in the (η_{AA}, η_{BB}) plane, which confirms that SOI typically arises when both species present weak or vanishing self-couplings, while its range of existence increases with Pe .

CCB-gas phase coexistence.—As we now show, the range of existence of CCB actually extends beyond that of SOI, since it may correspond to one of the phases involved in the phase-separation configurations following LOI. We now fix $\eta_{AA}^0 = \eta_{BB}^0 = -2$, $\eta_{AB}^0 = -\eta_{BA}^0 = 0.5$, $D_r = 0.1$, and perform simulations of the microscopic model (1) scanning the composition plane $(\bar{\rho}_A, \bar{\rho}_B)$.

The resulting phase diagram shown in Fig. 2(a) exhibits four distinctive lobes encircled by black dashed lines where static phase separation takes place [10], in qualitative agreement with the location of LSI in the linear stability diagram [blue regions in the inset of Fig. 2(a)]. Along the diagonal $\bar{\rho}_A = \bar{\rho}_B$ marked by a white dashed line in Fig. 2(a), the homogeneous phase becomes unstable below densities $\approx 2\rho_0$ and is superseded by the CCB phase [Fig. 2(b) and SMov 2] previously described. Further decreasing the densities, we observe system-spanning traveling bands for $\bar{\rho}_B \gtrsim \bar{\rho}_A$ and rotating spirals for $\bar{\rho}_B \lesssim \bar{\rho}_A$. Examples of these patterns are shown in the insets of Figs. 2(c) and 2(d) and SMov 2. Increasing the system size, the CCB phase remains qualitatively unchanged, as can be seen comparing the main panel and inset of Fig. 2(b). On the other hand, both traveling bands and spirals found at lower densities are replaced by a macroscopic CCB domain coexisting with a dilute homogeneous gas [Figs. 2(c) and 2(d)]. Accordingly, the locations of phase-separated CCB domains qualitatively correspond to regions of the composition plane where LOI is found [marked in magenta in the inset of Fig. 2(a)]. The system-wide CCB phase, on the other hand, borders

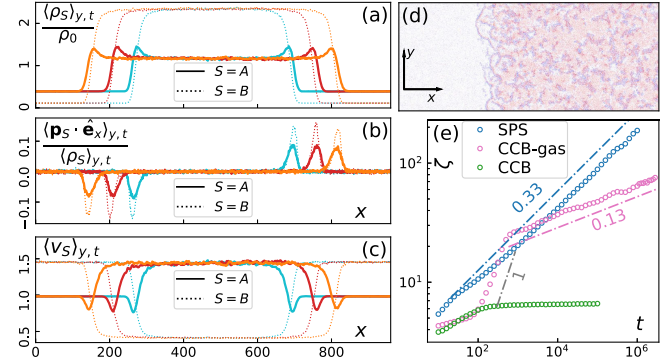


FIG. 3. (a)–(c) y - and time-averaged density (a), x component of the polarity (b) and speed (c) profiles for both species at various compositions along the tie line with $L_x = 6L_y = 960$. (d) CCB-gas interface for the configuration corresponding to the red curves in (a)–(c). (e) Typical domain size ζ evaluated from the first moment of the structure factor [51] as function of time for randomly initialized systems in the static phase separation (SPS), CCB-gas phase coexistence, and pure CCB regimes. For each curve in (a)–(c), the corresponding composition is marked by a symbol of the same color in Fig. 2(a).

the uniform high-density phase, in line with the location of SOI highlighted in green in the inset of Fig. 2(a).

To further characterize the CCB-gas coexistence phase, we performed simulations within this regime in a large rectangular domain. This way, the CCB domain connects with itself along the shortest dimension y , leading to a well-defined interface [Fig. 3(d)]. The y - and time-averaged density profiles shown in Fig. 3(a) indeed highlight two bulk phases of nearly constant densities. The values taken by $\langle \rho_{A,B} \rangle_{y,t}$ far away from the interfaces thus define a pair of points in the composition plane that can be joined by a tie line. Consistently with the usual picture of phase separation, shifting $(\bar{\rho}_A, \bar{\rho}_B)$ along this tie line changes the relative proportions of the gas and CCB phases while the corresponding bulk densities are left unchanged.

TRS is however obviously broken at mesoscopic scales in the CCB-gas coexistence phase, since chasing bands are constantly created in the dense CCB domain and expelled in the gas, where they quickly dissolve [Fig. 3(d) and SMov 3]. The outward mass flux from the chasing bands must then be balanced by the diffusive flux from the resulting excess particles in the gas, thereby maintaining the cohesion of the CCB domain. The nontrivial structure of the CCB-gas interface is also highlighted by the presence of local polarization pointing toward the dilute regions [Fig. 3(b)], at odds with the usual MIPS phenomenology [55,56]. We moreover note from Figs. 3(a) and 3(c) that A particles accumulate at interfaces where their self-propulsion speed is lowest, but move on average faster in the dense CCB domain than in the dilute gas.

Remarkably, the nonequilibrium nature of the CCB-gas phase coexistence also emerges over macroscopic scales, as

revealed by the anomalous coarsening behavior shown in Fig. 3(f). Although in the regimes of pure CCB and static phase separation the coarsening is arrested or follows the Lifshitz-Slyozov $t^{1/3}$ law [57] [green and blue symbols in Fig. 3(f)], the late-time coarsening of phase-separated CCB domains is characterized by an exponent ≈ 0.13 [magenta symbols in Fig. 3(f)], significantly smaller than the $\frac{1}{3}$ value expected in passive systems [58] and for the coarsening of dense MIPS domains [47–50,59]. We rationalize this result by noting that larger CCB domains generate more bands—and thus expel more mass into the surrounding gas—than smaller domains, which may naturally slow down coarsening [59].

Using a minimal model including self-propulsion and nonreciprocity, we have shown how the combination of these two sources of activity leads to a chaotic chasing band phase. Since it is involved in phase-separated configurations at large nonreciprocity, this phase is moreover found in a large portion of the phase diagram. Additionally, although the corresponding phase-separated domains are globally static, they still defy an equilibrium mapping as evidenced by the observed abnormal coarsening behavior. As they allow for the design of programmable quorum-sensing motility responses, both genetically engineered *E. coli* [61] and light-controlled microswimmers [38,62–64] offer promising experimental platforms to observe this new type of self-organized behavior.

We thank Xiaqing Shi and Hugues Chaté for their critical reading of our manuscript. This work has received support from the Max Planck School Matter to Life and the MaxSynBio Consortium, which are jointly funded by the Federal Ministry of Education and Research (BMBF) of Germany, and the Max Planck Society.

Appendix A: Simulations of the microscopic model.—Here, we give additional details on the microscopic model (1) and discuss the underlying assumptions behind its formulation. The Langevin equations (1) were integrated using the Euler-Maruyama scheme with time resolution $\Delta t = 0.1$.

The local density fields $\tilde{\rho}_S(\mathbf{r}, t)$ entering the expression of the quorum-sensing interaction in Eq. (1) were computed as $\tilde{\rho}_S(\mathbf{r}, t) = \sum_i \hat{w}(|\mathbf{r} - \mathbf{r}_{i,S}(t)|)$, with the linear weight function

$$\hat{w}(r) = \begin{cases} \frac{3}{\pi R^2} \left(1 - \frac{r}{R}\right) & \text{if } r < R, \\ 0 & \text{if } r \geq R, \end{cases}$$

that satisfies the normalization condition $\int_{\mathbb{R}^2} d\mathbf{r} \hat{w}(|\mathbf{r}|) = 1$. As mentioned in the main text, the dependency of the particles' self-propulsion speed with their density is modeled as $v_S(\tilde{\rho}_A, \tilde{\rho}_B) = v_0 L_{SA}(\tilde{\rho}_A) L_{SB}(\tilde{\rho}_B)$ with

$$L_{SS'}(x) \equiv 1 + \kappa \tanh\left(\frac{\eta_{SS'}^0 x - \rho_0}{\kappa \rho_0}\right).$$

Therefore, the reference density value ρ_0 satisfies $L_{SS'}(\rho_0) = 1$ and $\partial_x L_{SS'}(\rho_0) = \eta_{SS'}^0$. Here, κ controls the lower and upper limits of $L_{SS'}(x)$. To prevent jamming of particles at high densities, we set $\kappa = 0.7$ so that the minimum speed of species S is given by $\approx 0.09 v_0$.

To keep the microscopic model minimal, we have assumed a direct dependency of the particle motility in the local density fields. We expect this approximation to be well-verified for synthetic colloids controlled by optical feedback loops, which allow for a fast motility response to dynamical variations of the local density [23,38]. In the case of microorganisms communicating via chemical signals, the limit of instantaneous quorum-sensing response requires that the timescales associated with diffusion of chemicals and the internal gene regulatory network are fast as compared to the spatial dynamics of particles. Whether this assumption is verified depends on the system of interest, but the limit of fast quorum-sensing response should in general qualitatively capture the relevant dynamics [37].

Another simplification used in the microscopic model (1) consists in neglecting the short-range repulsive interactions between particles. This assumption is well-justified so long as the range of quorum-sensing interactions R is much larger than the typical particles size σ . In synthetic systems, R can be tuned arbitrarily, while $R = 10\sigma$ was used in Ref. [23]. In the case of quorum sensing regulated by chemicals, the scale R is set by the typical distance a signaling molecule can diffuse before being degraded. Estimates for the acyl-homoserine lactone molecules that mediate the quorum-sensing interactions of bacteria in Refs. [36,37] can reach a few millimeters [65], thus several orders of magnitude larger than the typical size of a bacterium.

Appendix B: The coarse-grained equations.—To derive the field theory describing the binary mixture of self-propelled particles with quorum-sensing interactions, we follow the coarse-graining framework developed for a single species [66]. As a starting point, we consider the many-body probability distribution $P(\mathbf{X}, t)$ with $\mathbf{X} \equiv \{\mathbf{r}_1, \mathbf{r}_2, \dots, \mathbf{r}_N, \theta_1, \theta_2, \dots, \theta_N\}$, and where N denotes the total number of particles of the two species. From the Langevin formulation (1), we get the statistically equivalent Fokker-Planck equation

$$\partial_t P = - \sum_{i=1}^N [\nabla_{\mathbf{r}_i} \cdot (v_{s_i} \hat{\mathbf{u}}(\theta_i) P) - D_i \partial_{\theta_i}^2 P], \quad (\text{B1})$$

where $\hat{\mathbf{u}}(\theta) = (\cos \theta, \sin \theta)$ and $s_i = A$ or B denotes the species of particle i . Without loss of generality, we set $s_i = A$ for $i = 1, 2, \dots, N_A$ and $s_i = B$ for $i = N_A + 1, N_A + 2, \dots, N$ with N_A the total number of A

particles. The one-particle probability densities $f_S(\mathbf{r}, \theta, t)$ are obtained from P by integrating over all degrees of freedom except that of one particle of species S . Hence, we have $f_A(\mathbf{r}_1, \theta_1, t) \equiv N_A \left(\prod_{i=2}^N \int d\mathbf{r}_i \int_0^{2\pi} d\theta_i \right) P(\mathbf{X}, t)$ while f_B is defined in a similar way. Integrating Eq. (B1) over the relevant coordinates, we thus determine the dynamics of the A and B single-particle distributions. For f_A (the generalization to the species B being straightforward), we obtain

$$\partial_t f_A(\mathbf{r}_1, \theta_1, t) = -\nabla_{\mathbf{r}_1} \cdot [\mathcal{G}_A(\mathbf{r}_1, \theta_1, t) \hat{\mathbf{u}}(\theta_1) f_A(\mathbf{r}_1, \theta_1, t)] + D_r \partial_{\theta_1}^2 f_A(\mathbf{r}_1, \theta_1, t), \quad (\text{B2})$$

where $\mathcal{G}_A(\mathbf{r}_1, \theta_1, t) \equiv \left(\prod_{k=2}^N \int d\mathbf{r}_k \right) v_A(\mathbf{X}_r) g_A(\mathbf{X}_r, \theta_1, t)$, and we have used the shorthand notation $\mathbf{X}_r \equiv \{\mathbf{r}_1, \dots, \mathbf{r}_N\}$. The function g_A is defined by $N_A \prod_{k=2}^N \int_0^{2\pi} d\theta_k P(\mathbf{X}, t) \equiv f_A(\mathbf{r}_1, \theta_1, t) g_A(\mathbf{X}_r, \theta_1, t)$. In general, the quorum-sensing interaction term \mathcal{G}_A in (B2) depends on the full many-body distribution. However, we now use the fact that the particle speed is formally a function of $\tilde{\rho}_{A,B}(\mathbf{X}_r)$, which in the mean field limit can be expressed in terms of the single particle densities:

$$\tilde{\rho}_S(\mathbf{X}_r) = \sum_j \hat{w}(|\mathbf{r}_1 - \mathbf{r}_j(t)|) \delta_{s_j, S} \simeq \int d\mathbf{r}' \hat{w}(|\mathbf{r}_1 - \mathbf{r}'|) \phi_S(\mathbf{r}', t) \equiv \tilde{\phi}_S(\mathbf{r}_1, t),$$

where the S particle density is formally defined as $\phi_S(\mathbf{r}, t) \equiv \int_0^{2\pi} d\theta f_S(\mathbf{r}, \theta, t)$. We expect this approximation to be reasonably valid in sufficiently dense systems. In the mean field limit considered here, the function v_A in the expression of \mathcal{G}_A thus only depends on the position variable \mathbf{r}_1 . Using that by definition $\left(\prod_{k=2}^N \int d\mathbf{r}_k \right) g_A(\mathbf{X}_r, \theta_1, t) = 1$, we therefore obtain the following after dropping indices on the \mathbf{r} and θ variables:

$$\partial_t f_S = -\nabla \cdot [v_S(\tilde{\phi}_A, \tilde{\phi}_B) \hat{\mathbf{u}}(\theta) f_S] + D_r \partial_{\theta}^2 f_S. \quad (\text{B3})$$

To simplify Eq. (B3) further, we use the local approximation $\tilde{\phi}_S(\mathbf{r}) \approx \phi_S(\mathbf{r})$, such that $v_S(\tilde{\phi}_A, \tilde{\phi}_B) \approx v_S(\phi_A, \phi_B)$.

Because of angular diffusion, we expect the dynamics of the system to be well-captured over long timescales by that of the low order orientational moments of the distributions f_A and f_B . Therefore, we expand the distribution f_S in angular Fourier modes: $f_S(\mathbf{r}, \theta, t) = (2\pi)^{-1} \sum_{k=-\infty}^{\infty} f_{k,S}(\mathbf{r}, t) \exp(-ik\theta)$. It is straightforward to check that the first three modes of f_S correspond to the complex representation of the density $\phi_S(\mathbf{r}, t)$, polarity $\mathbf{p}_S(\mathbf{r}, t)$ and nematic order $\mathbf{Q}_S(\mathbf{r}, t)$ fields. For the derivation

below, it is convenient to work with complex notations for which $\hat{\mathbf{u}}(\theta) \leftrightarrow e^{i\theta}$. We therefore define the complex gradient $\nabla \equiv \partial_x + i\partial_y$, and obtain from Eq. (B3)

$$\partial_t f_{k,S} = -\frac{1}{2} \nabla^* [v_S(\phi_A, \phi_B) f_{k+1,S}] - \frac{1}{2} \nabla [v_S(\phi_A, \phi_B) f_{k-1,S}] - D_r k^2 f_{k,S}, \quad (\text{B4})$$

where star denotes complex conjugate. The equation for the k th angular mode of f_S contains a linear damping term $-D_r k^2 f_{k,S}$. Considering the long time and large scale limits, we thus enslave the dynamics of the high order modes to that of the slow ones. As the densities are the only conserved fields, it is customary in this context to retain only them as hydrodynamic fields, while enslaving higher order modes [40]. Motivated by the presence of local polarization in the CCB phase, here we instead retain both ϕ_S and the polarity fields $\mathbf{p}_S(\mathbf{r}, t)$. Namely, neglecting $f_{k,S}$ for $k \geq 3$, we get from (B4) closed equations for $\phi_S, f_{1,S}$, and $f_{2,S}$. Setting $\partial_t f_{2,S} = 0$, we solve the equation for $f_{2,S}$, which leads to $f_{2,S} = -(8D_r)^{-1} \nabla (v_S f_{1,S})$. Replacing this expression in the equation for $f_{1,S}$, we get after going back to vector notations

$$\partial_t \phi_S = -\nabla \cdot (v_S \mathbf{p}_S), \quad (\text{B5a})$$

$$\partial_t \mathbf{p}_S = -\frac{1}{2} \nabla (v_S \phi_S) - D_r \mathbf{p}_S + \frac{v_S}{16D_r} \Delta (v_S \mathbf{p}_S) + (8D_r)^{-1} [\nabla (v_S \mathbf{p}_S)]_{\text{ST}} \cdot \nabla v_S, \quad (\text{B5b})$$

where $[\mathbf{A}]_{\text{ST}} \equiv \frac{1}{2} [\mathbf{A} + \mathbf{A}^T - \mathbf{I} \text{Tr}(\mathbf{A})]$ is the symmetric and traceless part of the tensor \mathbf{A} . Performing the linear stability analysis of Eqs. (B5) around their homogeneous disordered solution $\phi_S = \bar{\rho}_S$ and $\mathbf{p}_S = \mathbf{0}$, we obtain the results presented in the main text.

*Corresponding author: ramin.golestanian@ds.mpg.de

†Corresponding author: benoit.mahault@ds.mpg.de

- [1] P. Romanczuk, M. Bär, W. Ebeling, B. Lindner, and L. Schimansky-Geier, Active Brownian particles, *Eur. Phys. J. Special Topics* **202**, 1 (2012).
- [2] J. Prost, F. Jülicher, and J.-F. Joanny, Active gel physics, *Nat. Phys.* **11**, 111 (2015).
- [3] A. Doostmohammadi, J. Ignés-Mullol, J. M. Yeomans, and F. Sagués, Active nematics, *Nat. Commun.* **9**, 3246 (2018).
- [4] N. Uchida and R. Golestanian, Synchronization and Collective Dynamics in a Carpet of Microfluidic Rotors, *Phys. Rev. Lett.* **104**, 178103 (2010).
- [5] S. Fürthauer, M. Stempel, S. W. Grill, and F. Jülicher, Active chiral fluids, *Eur. Phys. J. E* **35**, 89 (2012).
- [6] D. Dell'Arciprete, M. L. Blow, A. T. Brown, F. D. C. Farrell, J. S. Lintuvuori, A. F. McVey, D. Marenduzzo, and W. C. K.

- Poon, A growing bacterial colony in two dimensions as an active nematic, *Nat. Commun.* **9**, 4190 (2018).
- [7] R. Golestanian, Phoretic active matter, in *Active Matter and Nonequilibrium Statistical Physics: Lecture Notes of the Les Houches Summer School: Volume 112, September 2018* (Oxford University Press, New York, 2022), 10.1093/oso/9780192858313.001.0001.
- [8] G. Gompper *et al.*, The 2020 motile active matter roadmap, *J. Phys. Condens. Matter* **32**, 193001 (2020).
- [9] A. V. Ivlev, J. Bartnick, M. Heinen, C.-R. Du, V. Nosenko, and H. Löwen, Statistical Mechanics Where Newton's Third Law Is Broken, *Phys. Rev. X* **5**, 011035 (2015).
- [10] S. Saha, J. Agudo-Canalejo, and R. Golestanian, Scalar Active Mixtures: The Nonreciprocal Cahn-Hilliard Model, *Phys. Rev. X* **10**, 041009 (2020).
- [11] Z. You, A. Baskaran, and M. C. Marchetti, Nonreciprocity as a generic route to traveling states, *Proc. Natl. Acad. Sci. U.S.A.* **117**, 19767 (2020).
- [12] M. Fruchart, R. Hanai, P. B. Littlewood, and V. Vitelli, Nonreciprocal phase transitions, *Nature (London)* **592**, 363 (2021).
- [13] D. Gelbwaser-Klimovsky, N. Graham, M. Kardar, and M. Krüger, Near Field Propulsion Forces from Nonreciprocal Media, *Phys. Rev. Lett.* **126**, 170401 (2021).
- [14] J. Dzubiella, H. Löwen, and C. N. Likos, Depletion Forces in Nonequilibrium, *Phys. Rev. Lett.* **91**, 248301 (2003).
- [15] R. Soto and R. Golestanian, Self-Assembly of Catalytically Active Colloidal Molecules: Tailoring Activity through Surface Chemistry, *Phys. Rev. Lett.* **112**, 068301 (2014).
- [16] A. Wysocki, R. G. Winkler, and G. Gompper, Propagating interfaces in mixtures of active and passive Brownian particles, *New J. Phys.* **18**, 123030 (2016).
- [17] R. Wittkowski, J. Stenhammar, and M. E. Cates, Nonequilibrium dynamics of mixtures of active and passive colloidal particles, *New J. Phys.* **19**, 105003 (2017).
- [18] J. Agudo-Canalejo and R. Golestanian, Active Phase Separation in Mixtures of Chemically Interacting Particles, *Phys. Rev. Lett.* **123**, 018101 (2019).
- [19] B. Nasouri and R. Golestanian, Exact Phoretic Interaction of Two Chemically Active Particles, *Phys. Rev. Lett.* **124**, 168003 (2020).
- [20] J. P. Banerjee, R. Mandal, D. S. Banerjee, S. Thutupalli, and M. Rao, Unjamming and emergent nonreciprocity in active ploughing through a compressible viscoelastic fluid, *Nat. Commun.* **13**, 1 (2022).
- [21] R. K. Gupta, R. Kant, H. Soni, A. K. Sood, and S. Ramaswamy, Active nonreciprocal attraction between motile particles in an elastic medium, *Phys. Rev. E* **105**, 064602 (2022).
- [22] Q.-s. Chen, A. Patelli, H. Chaté, Y.-q. Ma, and X.-q. Shi, Fore-aft asymmetric flocking, *Phys. Rev. E* **96**, 020601(R) (2017).
- [23] T. Bäuerle, A. Fischer, T. Speck, and C. Bechinger, Self-organization of active particles by quorum sensing rules, *Nat. Commun.* **9**, 3232 (2018).
- [24] L. Gómez-Nava, R. Bon, and F. Peruani, Intermittent collective motion in sheep results from alternating the role of leader and follower, *Nat. Phys.* **18**, 1494 (2022).
- [25] R. El-Ganainy, K. G. Makris, M. Khajavikhan, Z. H. Musslimani, S. Rotter, and D. N. Christodoulides, Non-Hermitian physics and PT symmetry, *Nat. Phys.* **14**, 11 (2018).
- [26] S. Shankar, A. Souslov, M. J. Bowick, M. C. Marchetti, and V. Vitelli, Topological active matter, *Nat. Rev. Phys.* **4**, 380 (2022).
- [27] T. Frohoff-Hülsmann, J. Wrembel, and U. Thiele, Suppression of coarsening and emergence of oscillatory behavior in a Cahn-Hilliard model with nonvariational coupling, *Phys. Rev. E* **103**, 042602 (2021).
- [28] V. Ouazan-Reboul, J. Agudo-Canalejo, and R. Golestanian, Non-equilibrium phase separation in mixtures of catalytically active particles: Size dispersity and screening effects, *Eur. Phys. J. E* **44**, 113 (2021).
- [29] S. A. M. Loos, S. H. L. Klapp, and T. Martynec, Long-Range Order and Directional Defect Propagation in the Nonreciprocal XY Model with Vision Cone Interactions, *Phys. Rev. Lett.* **130**, 198301 (2023).
- [30] S. Saha and R. Golestanian, Effervescent waves in a binary mixture with non-reciprocal couplings, [arXiv:2208.14985](https://arxiv.org/abs/2208.14985).
- [31] J. W. Cahn and J. E. Hilliard, Free energy of a nonuniform system. I. Interfacial free energy, *J. Chem. Phys.* **28**, 258 (2004).
- [32] X. Diego, L. Marcon, P. Müller, and J. Sharpe, Key Features of Turing Systems Are Determined Purely by Network Topology, *Phys. Rev. X* **8**, 021071 (2018).
- [33] P. A. Haas and R. E. Goldstein, Turing's Diffusive Threshold in Random Reaction-Diffusion Systems, *Phys. Rev. Lett.* **126**, 238101 (2021).
- [34] T. Frohoff-Hülsmann, U. Thiele, and L. M. Pismen, Nonreciprocity induces resonances in a two-field Cahn-Hilliard model, *Phil. Trans. R. Soc. A* **381**, 20220087 (2023).
- [35] R. Daniels, J. Vanderleyden, and J. Michiels, Quorum sensing and swarming migration in bacteria, *FEMS Microbiol. Rev.* **28**, 261 (2004).
- [36] C. Liu, X. Fu, L. Liu, X. Ren, C. K. Chau, S. Li, L. Xiang, H. Zeng, G. Chen, L.-H. Tang, P. Lenz, X. Cui, W. Huang, T. Hwa, and J.-D. Huang, Sequential establishment of stripe patterns in an expanding cell population, *Science* **334**, 238 (2011).
- [37] A. Curatolo, N. Zhou, Y. Zhao, C. Liu, A. Daerr, J. Tailleur, and J. Huang, Cooperative pattern formation in multi-component bacterial systems through reciprocal motility regulation, *Nat. Phys.* **16**, 1152 (2020).
- [38] J. R. Gomez-Solano, S. Samin, C. Lozano, P. Ruedas-Batuecas, R. van Roij, and C. Bechinger, Tuning the motility and directionality of self-propelled colloids, *Sci. Rep.* **7**, 14891 (2017).
- [39] F. A. Lavergne, H. Wendehenne, T. Bäuerle, and C. Bechinger, Group formation and cohesion of active particles with visual perception-dependent motility, *Science* **364**, 70 (2019).
- [40] M. E. Cates and J. Tailleur, Motility-induced phase separation, *Annu. Rev. Condens. Matter Phys.* **6**, 219 (2015).
- [41] A. P. Solon, J. Stenhammar, M. E. Cates, Y. Kafri, and J. Tailleur, Generalized thermodynamics of motility-induced phase separation: Phase equilibria, laplace pressure, and change of ensembles, *New J. Phys.* **20**, 075001 (2018).

- [42] A. Fischer, F. Schmid, and T. Speck, Quorum-sensing active particles with discontinuous motility, *Phys. Rev. E* **101**, 012601 (2020).
- [43] A. Dinelli, J. O'Byrne, A. Curatolo, Y. Zhao, P. Sollich, and J. Tailleur, Non-reciprocity across scales in active mixtures, [arXiv:2203.07757](https://arxiv.org/abs/2203.07757).
- [44] Y.-J. Chiu and A. K. Omar, Phase coexistence implications of violating Newton's third law, *J. Chem. Phys.* **158** (2023).
- [45] R. Mandal, S. S. Jaramillo, and P. Sollich, Robustness of travelling states in generic non-reciprocal mixtures, [arXiv:2212.05618](https://arxiv.org/abs/2212.05618).
- [46] K. L. Kreienkamp and S. H. L. Klapp, Clustering and flocking of repulsive chiral active particles with non-reciprocal couplings, *New J. Phys.* **24**, 123009 (2022).
- [47] J. Stenhammar, D. Marenduzzo, R. J. Allen, and M. E. Cates, Phase behaviour of active Brownian particles: The role of dimensionality, *Soft Matter* **10**, 1489 (2014).
- [48] C. B. Caporusso, P. Digregorio, D. Levis, L. F. Cugliandolo, and G. Gonnella, Motility-Induced Microphase and Macrophase Separation in a Two-Dimensional Active Brownian Particle System, *Phys. Rev. Lett.* **125**, 178004 (2020).
- [49] X.-q. Shi, G. Fausti, H. Chaté, C. Nardini, and A. Solon, Self-Organized Critical Coexistence Phase in Repulsive Active Particles, *Phys. Rev. Lett.* **125**, 168001 (2020).
- [50] C. B. Caporusso, L. F. Cugliandolo, P. Digregorio, G. Gonnella, D. Levis, and A. Suma, Dynamics of Motility-Induced Clusters: Coarsening beyond Ostwald Ripening, *Phys. Rev. Lett.* **131**, 068201 (2023).
- [51] See Supplemental Material at <http://link.aps.org/supplemental/10.1103/PhysRevLett.131.148301> for further details.
- [52] SOI is forbidden in standard binary reaction-diffusion systems [32] but can occur under certain conditions, such as systems on curved surfaces [53] or in the presence of differential flow [54].
- [53] R. Nishide and S. Ishihara, Pattern Propagation Driven by Surface Curvature, *Phys. Rev. Lett.* **128**, 224101 (2022).
- [54] A. B. Rovinsky and M. Menzinger, Chemical Instability Induced by a Differential Flow, *Phys. Rev. Lett.* **69**, 1193 (1992).
- [55] A. K. Omar, Z.-G. Wang, and J. F. Brady, Microscopic origins of the swim pressure and the anomalous surface tension of active matter, *Phys. Rev. E* **101**, 012604 (2020).
- [56] B. Mahault, P. Godara, and R. Golestanian, Emergent organization and polarization due to active fluctuations, *Phys. Rev. Res.* **5**, L022012 (2023).
- [57] I. Lifshitz and V. Slyozov, The kinetics of precipitation from supersaturated solid solutions, *J. Phys. Chem. Solids* **19**, 35 (1961).
- [58] A. J. Bray, Theory of phase-ordering kinetics, *Adv. Phys.* **51**, 481 (2002).
- [59] We note that for an underdamped dynamics the mapping of MIPS to an equilibrium coarse-grained model at large scales may not hold [60].
- [60] S. Mandal, B. Liebchen, and H. Löwen, Motility-Induced Temperature Difference in Coexisting Phases, *Phys. Rev. Lett.* **123**, 228001 (2019).
- [61] L. E. Weiss, J. P. Badalamenti, L. J. Weaver, A. R. Tascone, P. S. Weiss, T. L. Richard, and P. C. Cirino, Engineering motility as a phenotypic response to luxI/r-dependent quorum sensing in *Escherichia coli*, *Biotechnol. Bioeng.* **100**, 1251 (2008).
- [62] A. P. Bregulla, H. Yang, and F. Cichos, Stochastic localization of microswimmers by photon nudging, *ACS Nano* **8**, 6542 (2014).
- [63] H. Massana-Cid, C. Maggi, G. Frangipane, and R. Di Leonardo, Rectification and confinement of photokinetic bacteria in an optical feedback loop, *Nat. Commun.* **13**, 2740 (2022).
- [64] S. Yang, M. Huang, Y. Zhao, and H. P. Zhang, Controlling Cell Motion and Microscale Flow with Polarized Light Fields, *Phys. Rev. Lett.* **126**, 058001 (2021).
- [65] M. Marena, M. Zanardo, A. Trovato, F. Seno, and A. Squartini, Modeling quorum sensing trade-offs between bacterial cell density and system extension from open boundaries, *Sci. Rep.* **6**, 39142 (2016).
- [66] M. te Vrugt, J. Bickmann, and R. Wittkowski, How to derive a predictive field theory for active Brownian particles: A step-by-step tutorial, *J. Phys. Condens. Matter* **35**, 313001 (2023).